Ceramics International 43 (2017) 2252–2266

Contents lists available at ScienceDirect

Ceramics International

journal homepage: www.elsevier.com/locate/ceramint

Strain-induced multiscale structural changes in lamellar thermal barrier coatings

Guang-Rong Li, Guan-Jun Yang*, Cheng-Xin Li, Chang-Jiu Li

State Key Laboratory for Mechanical Behavior of Materials, School of Materials Science and Engineering, Xi'an Jiaotong University, No. 28 Xianning West Road, Xi'an, Shaanxi Province 710049, PR China

ARTICLE INFO

Keywords:
Plasma spraying
Multiscale structural changes
Thermal barrier coatings
Mechanical properties
CTE mismatch strain

ABSTRACT

The thermal mismatch stress, as well as residual stress, in coating/substrate systems often leads to structural changes and subsequent coating debonding in the systems. This study focused on the changes induced in the microstructure and properties of lamellar yttria-stabilized zirconia coatings upon heating, with the aim of elucidating their starting microstructure prior to sintering. The results showed that the combined effect of the residual stress and the thermal mismatch stress results in scale-sensitive changes in the properties of the coatings. The macroscale properties changed significantly, while the microscale properties changed only slightly. Structural characterization revealed that a certain degree of expansion at the tips of both the intersplat pores and the intrasplat cracks occurs, contributing to the microscale structural changes observed in most regions. Moreover, a few mesoscale cracks covering several layers were also observed. A lamellar structural model was developed to correlate the multiscale structural changes observed with those in the properties. Finally, this study revealed that the actual starting structure of plasma-sprayed thermal barrier coatings prior to sintering is different from that in the as-deposited state. This should aid in obtaining an in-depth understanding on the microstructural and properties evolution of the constrained coatings under actual service conditions.

1. Introduction

Over past few decades, thermal barrier coatings (TBCs) have been widely used in gas turbines and diesel engines to protect hot-section metallic components (e.g., combustion cans, blades and vanes) [1–4]. Yttria-stabilized zirconia (YSZ) continues to dominate the material choice of the ceramic top coat of TBCs owing to its low thermal conductivity and high thermal expansion coefficient [5–7]. In addition to the attractive intrinsic properties of YSZ, plasma sprayed YSZ coatings (PS-YSZ) further exhibit excellent functional properties owing to its unique porous structure, which is formed because of the spraying process [8,9]. During thermal spraying, a stream of fully molten or partially molten particles impact on substrate successively, following by flattening, rapid solidification and cooling. Subsequently, the obtained coating exhibits a lamellar structure with overlapped splats lying nearly parallel to substrate [10]. Moreover, the unique porous structure is primarily attributed to the presence of a two-dimensional (2D) pore network [11–13], in which intersplat pores are connected with intrasplat cracks. The intersplat pores result from imperfect bonding between lamellar splats. That's why the plasma sprayed ceramic coatings exhibit an intersplat bonding ratio range of 10–32% without special preheating [10,14]. Moreover, the intersplat pores are roughly parallel to substrate surface. The intrasplat cracks are generated from the splat quenching. Consequently, the disk-shaped splats are divided into several splat segments by those through-thickness intrasplat cracks [12]. These 2D cracks play a crucial role with respect to the thermal insulation properties and strain tolerance of TBCs, which show superior durability under severe thermal cycling conditions [15,16]. As a consequence, this unique pore network confers $>1/2$ drop of through-thickness thermal conductivity (~1 W m^{-1} K^{-1}) [17–19] and approximately $>1/2$ decrease of in-plane elastic modulus [6,20–22] with respect to the bulk YSZ material.

The high operating temperature of engines often has a detrimental effect on PS-YSZ coatings, resulting, in particular, in sintering-induced in-plane stiffening as well as an increase in the through-thickness thermal conductivity. The former will compromise the strain tolerance of the PS-YSZ, whilst the latter reduces its thermal insulating capability. Therefore, significant efforts have been made to examine the dynamic evolution of the microstructure and thermal/mechanical properties of PS-YSZ coating during thermal exposure from various perspectives [9,11,16,18,23–25]. Among these study, isothermal heat treatment attracted quite amount of attentions owing to its conve-

* Corresponding author.
E-mail address: ygj@mail.xjtu.edu.cn (G.-J. Yang).

http://dx.doi.org/10.1016/j.ceramint.2016.11.009
Received 27 September 2016; Received in revised form 31 October 2016; Accepted 2 November 2016
Available online 04 November 2016

nience for the accelerated aging to acquire relevant regularity. It has been reported that, in general, the porous structure of such coatings becomes denser with the cracks healing up [7,11,26,27]. Further, the sharp increase in the corresponding properties (i.e., thermal conductivity [9,17,18,28] as well as elastic modulus [16,17,25,27,29]) at initial heating stage slows down for extended thermal exposure. In other words, with extended thermal exposure, the changes in the physical properties become less extensive. Anderson et al. [25] separated the crack healing and phase transformation at different temperatures through impedance spectroscopy. It is believed that phase transformation of the PS-YSZ coatings tends to be significant at a higher aging temperature (i.e., > 1200 °C) [27,29,30]. In addition to the evolution of microstructure and functional properties, some other investigations focused on revealing the sintering characteristics of the PS-YSZ coatings coherent to some intrinsic behaviors of the YSZ material. Chen et al. [24] examined the temperature-dependent grain growth rates. Erk et al. [31] revealed that different diffusion mechanisms are responsible dominantly for the healing of 2D pores at different temperatures.

The above-described investigations presented a distinct effect of thermal exposure on the performance degradation of the PS-YSZ coatings. However, these studies were all based on free-standing YSZ coatings for two reasons. Firstly, by studying the free-standing coatings, one can investigate the sintering effects of the top coat on the failure mechanism, while avoiding the growth of a thermally grown oxide layer [32,33]. Secondly, the free-standing YSZ coatings often allow for measurements of the thermal conductivity using a frequently-used method, namely, the laser flash technique [9,18,23,27,28]. Nevertheless, the observed changes in the structure and properties do not accurately represent the actual conditions since the coatings are still attached to the substrate. There have been a few studies on coating/substrate systems [15,34]. However, most of them focused on the failure mechanism during the cooling stage. Thompson et al. [21] studied the evolution of the microstructure and properties of coatings still attached to the substrate during thermal exposure and reported that free-standing YSZ coatings exhibit significantly greater changes in their mechanical properties than do constrained coatings. Therefore, the sintering-induced stiffness of free-standing coatings is overestimated compared to the actual value.

There may be two reasons for the difference in the values mentioned above. The first could be the fact that the sintering process is constrained in the case of constrained coatings [35–38]. Given the constraint placed by the much stiffer substrate, these coatings show a lower densification rate as well as slower sintering kinetics. The second reason can be the differences in the starting states of these two types of coatings prior to the sintering process [11,39]. In the case of TBCs, the mismatch in the thermal expansion coefficients (CTEs) of the YSZ coating (approximately $11{\cdot}10^{-6}$ K^{-1}) and the substrate (approximately $15{\cdot}10^{-6}$ K^{-1} for a Ni-based superalloy) leads to an increase in the strain on the coating. This strain may further change the porous structure of the coating during heating stage. Cipitria et al. [39] developed a model to predict the sintering characteristics of constrained coatings based on the temperature-dependent CTE mismatch stress and the time-dependent constrained contraction stress. They dealt with these two kinds of stresses as a sum of stored elastic strain energy. However, the essential structural changes resulting from the CTE mismatch strain and the effect of the resulting structure on sintering for longer durations remain unknown.

There is no doubt that the starting structure significantly affects the sintering behavior of TBCs. Tan et al. [19] showed that a higher initial porosity often leads to smaller increases in the thermal conductivity in the case of annealed coatings. Similarly, Chi et al. [18] confirmed that a higher porosity of TBCs often corresponds to a lower sintering kinetics, despite undergoing isothermal exposure or thermal cyclic test. Moreover, their work [18] revealed that the nature of the pores and interfaces plays a crucial role during the sintering process. For instance, longer and wider inter/intrasplat pores may retard the sintering process. Other studies focusing on the evolution of the mechanical properties (i.e., the Young's modulus [40] and fracture toughness [41]) have also shown that different preprocessing-induced starting structures result in different sintering behaviors. To summarize, these investigations suggested that the starting structure of PS-YSZ coatings has a marked effect on their sintering behavior. Consequently, it is necessary to determine the actual starting structure of PS-YSZ coatings prior to sintering by studying the evolution of their microstructure and properties during the initial heating stage.

In this study, we aimed to study the strain-induced structural changes in coating/substrate systems. The heating-induced evolution of the microstructure and properties of PS-YSZ coatings attached to substrates was examined experimentally. A general structural model was developed to explore the effects of the induced structural changes on the mechanical properties of the coatings. This study can be the foundation for further research on the constrained sintering of TBCs for longer periods, since it distinguishes the actual initial sintering state from the commonly assumed free-standing as-deposited state.

2. Experimental

2.1. General background and experimental design

As a beforehand work, it is necessary to analysis the possible stress/strain existing in the coatings bonded to substrate. The residual stress (called factor no. 1) and the CTE mismatch strain (called factor no. 2) are the two main driving forces responsible for the structural changes induced in TBCs. The residual stress (including the quenching stress and thermal stress) is generated during deposition process [42,43]. Due to the splat cooling contraction, the disk-shaped splats are divided into several segments by intrasplat cracks, which relax the quenching stress from theoretical GPa to tens of MPa. The CTE mismatch strain arises from the subsequently thermal cycling process [11,39]. In the case of a typical TBC system, the substrate has a higher CTE (approximately $15{\cdot}10^{-6}$ K^{-1} for a Ni-based superalloy [11]) than that of the YSZ coating (approximately $11{\cdot}10^{-6}$ K^{-1} [38]). Consequently, the residual stress and the CTE mismatch strain are more likely to be positive in YSZ coatings deposited at room temperature [43]. Schematics of a free-standing coating and a coating attached to the substrate are shown in Fig. 1(a, b). It can be seen clearly that the free-standing coating does not experience the CTE mismatch strain or exhibit the residual stress. In contrast, the changes induced in the structure of the coating attached to the superalloy substrate are probably attributable to both the residual stress and the CTE mismatch strain. Accordingly, when designing experiments, it is necessary to study the heating-induced structural and properties changes of the YSZ coatings on substrates with or without a CTE mismatch, in order to be able to distinguish the separate effect of the different stress resources, as shown in Fig. 1c.

2.2. Experimental materials

Based on the experimental design described above, two types of coating/substrate systems were used in this study. The first one consisted of a YSZ coating and a YSZ bulk substrate and did not exhibit a CTE mismatch. The other one consisted of a YSZ coating and a Ni-based superalloy or bulk magnesia substrate with a higher CTE. As for a comparison, YSZ coating was also deposited on stainless steel to obtain a free-standing coating through post-spray dissolution of the substrate by a hydrochloric acid. A commercially available hollow spheroidized 8 wt% YSZ powder (HOSP, −75 to +45 μm, Metco 204B-NS, Sulzer Metco Inc., New York, USA) was used to prepare the YSZ coatings. In addition to the coatings, individual YSZ splats were also formed on the bulk YSZ and magnesia substrate, in order to investigate the fundamental changes in the structure of plasma-sprayed YSZ.

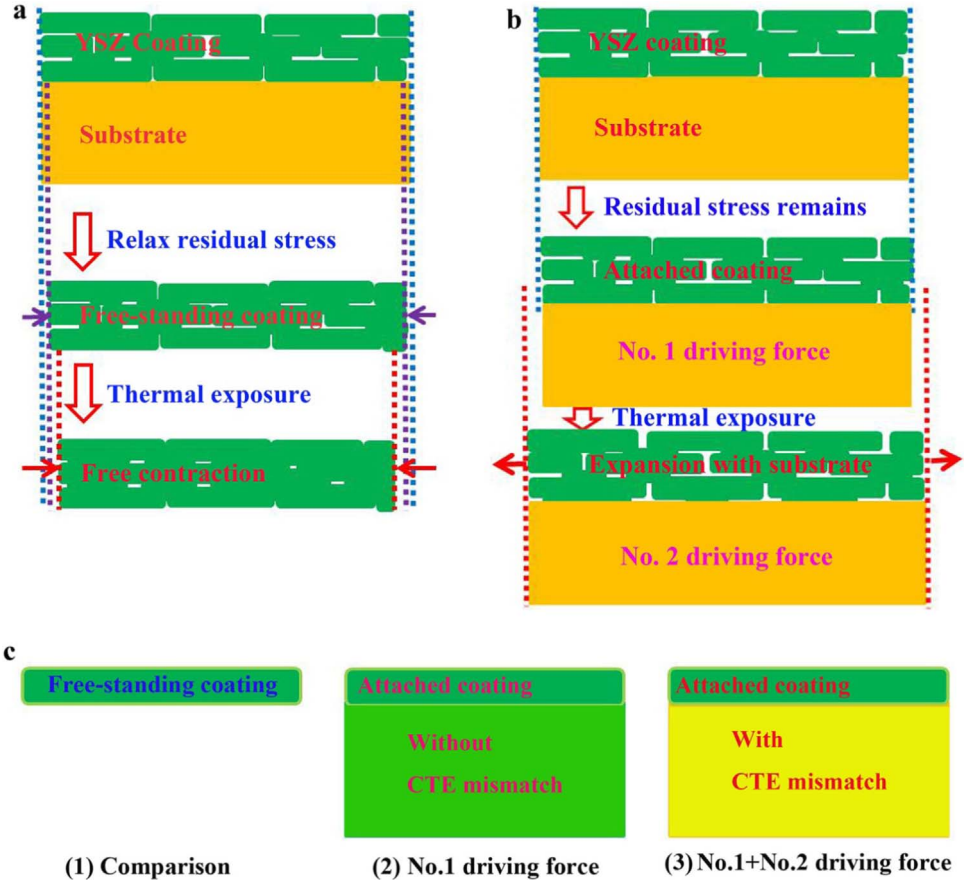

Fig. 1. Schematics comparing the stress-affected states of YSZ coatings detached from substrates and YSZ coatings attached to substrates: (a) free-standing coating, (b) YSZ coating attached to substrate, and (c) an experimental design based on the analysis of the effects of stress.

Before the top-coat deposition, a bond-coat with NiCoCrAlTaY (~37 μm, Amdry 997, Sulzer Metco, New York, USA) was deposited preferentially on substrate to make sure a good adhesion between substrate and top-coat.

2.3. Sample preparation and heating test

The YSZ top-coat was deposited to a thickness of approximately 500 μm using a commercial air plasma spray (APS) system (GP-80, 80 kW class, Jiujiang, China). In order to melt spraying particles sufficiently, an internal powder feeding nozzle was used in this study. The bond-coat was deposited by low pressure plasma spraying (LPPS) to a thickness of approximately 100 μm. After the deposition of bond-coat, a pre-annealing treatment was carried out in an argon atmosphere at 1000 °C for 4 h followed by further annealing at 1080 °C for 4 h to grow a uniform and dense α-Al_2O_3-based thermally grown oxidation (TGO) [44]. The spraying parameters of APS and LPPS were shown in Table 1.

Table 1
Spraying parameters of APS and LPPS.

Parameters	LPPS	APS
Plasma arc voltage/V	72	70
Plasma arc current/A	620	600
Flow rate of primary gas (Ar)/L min^{-1}	40	50
Flow rate of secondary gas (H_2)/L min^{-1}	8	7
Flow rate of powder feeding gas/L min^{-1}	Ar/2	N_2/7
Chamber pressure/kPa	15	/
Spray distance/mm	160	80
Torch traverse speed/mm s^{-1}	100	800

In order to focus on the changes in the structure and properties before sintering, all the samples were subjected to thermal cycling for one cycle. During this cycle, the samples were heated to 1100 °C at 20 °C/min, held at this temperature for 5 min, and then cooled. For simplification, the coatings (individual splats) bonded to the YSZ substrates, the magnesia substrates, the Ni-based superalloy substrates are referred to as Attached-to-YSZ, Attached-to-Mg, and Attached-to-Ni samples, respectively.

2.4. Microstructural characterization and measurement of properties

Quasi-in-situ morphological observations were made using a scanning electron microscopy (SEM) system (TESCAN MIRA 3, Czech). Cross-sectional samples of the individual splats and YSZ coatings were prepared using a focused ion beam system (Helios Nano Lab 600i dual-beam, America), in order to prevent damage to the initially present bonds. The apparent porosity of the samples was determined by image analysis using SEM backscattered electron images at a magnification of ×1000. At least ten images were used to estimate the porosity of each sample. The 2D pore length density, defined as the total length of 2D pores in unit area, was determined using polished samples by a previously described procedure [45]. The densities of intersplat pores and intrasplat cracks were obtained from the polished cross-section and surface, respectively. For each sample, at least 20 SEM images at a magnification of ×5000 were used. The obtained intersplat pore density was used to estimate the interlamellar bonding ratio, defined as the ratio of the bonding area to the lamellae area, through the following expressions [45,46]:

$$L_2 = \frac{HL_1}{\delta} \quad (1)$$

$$\varepsilon = \frac{\xi H L_1}{L_2} = \xi\delta \tag{2}$$

$$\alpha = (1 - \varepsilon) \times 100\% \tag{3}$$

where H and L_1 refer to the coating thickness and length, respectively; L_2 is the total length of the interface between the splats in the coating; δ is the mean splat thickness; ξ is the residual 2D pore length density; ε is the interlamellar unbonded ratio attributable to the 2D pores; and α is the interlamellar bonding ratio.

Another way of determining the bonding ratio of thermally sprayed coatings is through the structural visualization described elsewhere [46]. This involves having an $Al(NO_3)_3$ saturated solution infiltrate into the YSZ coating being examined, following by drying and heat treatment from room temperature to 550 °C. Then, using energy-disperse X-ray spectroscopy, the mean lamellar bonding ratio can be determined.

The macroscopic elastic moduli in the in-plane direction was measured using both a three-point bending test system (Instron 5943, America) [47] and a microforce tensile test system performed at a cross-head speed of 10–4 mm/s (MTS Tytron 250, America) [48]. In the case of the three-point bending test, the elastic modulus of the coating can be calculated from the stress-strain behavior of the specimen. During the bending test, the central deflection w can be expressed as [47]:

$$w = \frac{PL^3}{48D} \tag{4}$$

$$D = \frac{Eh^3}{12(1 - \nu^2)} \tag{5}$$

where P is the load applied to the middle of the span, L is the span between two supports, D is the bending stiffness, E is the elastic modulus of the coating, h is the coating thickness, ν is the Poisson's ratio of the coating (taken as 0.1 in this study [34]).

In the case of the microforce tensile test, uniaxial tensile testing was performed. The force and displacement were automatically recorded by a high-resolution laser detecting system. Then the elastic modulus can be obtained from the initial linear stress-strain curve of the coating.

Knoop hardness tests (Buehler Micromet 5104, Akashi Corporation, Japan) [49] were performed at a test load of 300 g and holding time of 30 s, with the aim to measure the microscale elastic moduli of the YSZ coatings. Knoop indentation is based on the measurement of the elastic recovery of the in-surface dimensions of Knoop indentations. During unloading, the elastic recovery reduces the length of the minor diagonal of the indentation impression (b'), while the length of the major diagonal of the indentation impression (a') remains relatively unaffected. The ratio of the major (a) to minor (b) diagonals of the Knoop indenter is 7.11. The formula for determining the elastic modulus is:

$$E = \frac{\alpha H}{(\frac{b}{a} - \frac{b'}{a'})} \tag{6}$$

where α is a constant (0.45), H is hardness, a' and b' are the lengths of the major and minor diagonals of the indentation impression, respectively, and b/a is 1/7.11.

It is clear that the Knoop indentation measurement is based on the elastic recovery of the minor diagonal. In order to obtain the in-plane elastic modulus of the coating, the direction of the elastic recovery of the minor diagonal should be parallel to the in-plane direction (coating surface). In contrast, the direction of the elastic recovery of the minor diagonal should be vertical to the in-plane direction, with the aim to obtain the out-plane elastic modulus of the coating, as shown in Fig. 2. Therefore, the in-plane and the out-plane elastic modulus can be obtained by performing Knoop indentation test on the polished surface and cross-section, respectively.

The ionic conductivities were measured using a potentiostat (Solartron SI1287, Hampshire, England) by a previously described direct current method [50]. In the case of the ionic conductivity measurement in out-plane direction with a circular sample (φ20 mm×0.5 mm), a platinium slurry was pasted uniformly in an area of φ8 mm on both sides of the sample, ensuring that the centers of these two circles are well coupled. The pasted samples were dried at 100 °C for 30 min prior to heat in a furnace with a heating rate of 5 °C/min to 850 °C holding for 30 min to solidify platinum paste. The counter electrodes and working electrode were connected to these two platinum sides, respectively. The resistivity and then the ionic conductivity of YSZ coatings can be calculated according to the linear relation between current and potential difference. In the case of the ionic conductivity in in-plane direction, a simplified four-terminal method was used in this study [51]. The specimens were pasted with four terminals using platinum glue and cured as in the case of the circular specimens.

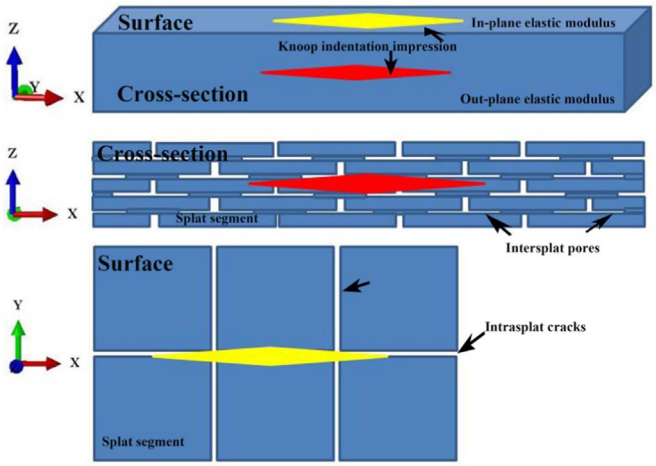

Fig. 2. Schematics to obtain the in-plane and the out-plane elastic modulus by Knoop indentation test.

To determine the gas leakage rate, a circular sample (φ20 mm×0.5 mm) was connected to a vacuum chamber with a pressure gauge and pumped down to a vacuum condition. The gas permeability across the sample was estimated from the relationship between the pressure difference across the two sides of the test samples and leakage time once the evacuation process had been stopped. The configuration of testing set can be found elsewhere [52].

3. Results

3.1. Evolution of properties after heating

Fig. 3 shows the evolution of the properties of the various samples after heating. As for a comparison, normalized properties for those samples after heating with respect to the corresponding as-deposited state are also presented in Fig. 3. In the case of the elastic modulus (see Fig. 3a), both the macroscale and the microscale elastic modulus in in-plane direction showed similar evolutionary trends after the samples had been heating. The free-standing coatings showed a slight increase in their moduli, while the Attached-to-YSZ coatings showed a slight decrease. Moreover, the decrease was more significant in the case of the Attached-to-Ni coatings. Another noteworthy phenomenon with respect to the different measurement scales was that heating resulted in a much sharper drop in the macroscale elastic modulus as compared to the microscale elastic modulus for the Attached-to-Ni coatings. However, the decreases in the macroscale and microscale moduli were comparable for the Attached-to-YSZ coatings, (see Fig. 3(a-2)). This meant that structural changes were induced both at the micro and at the macroscale in the Attached-to-Ni coatings after heating.

The thermal conductivity of a top coat attached to a substrate

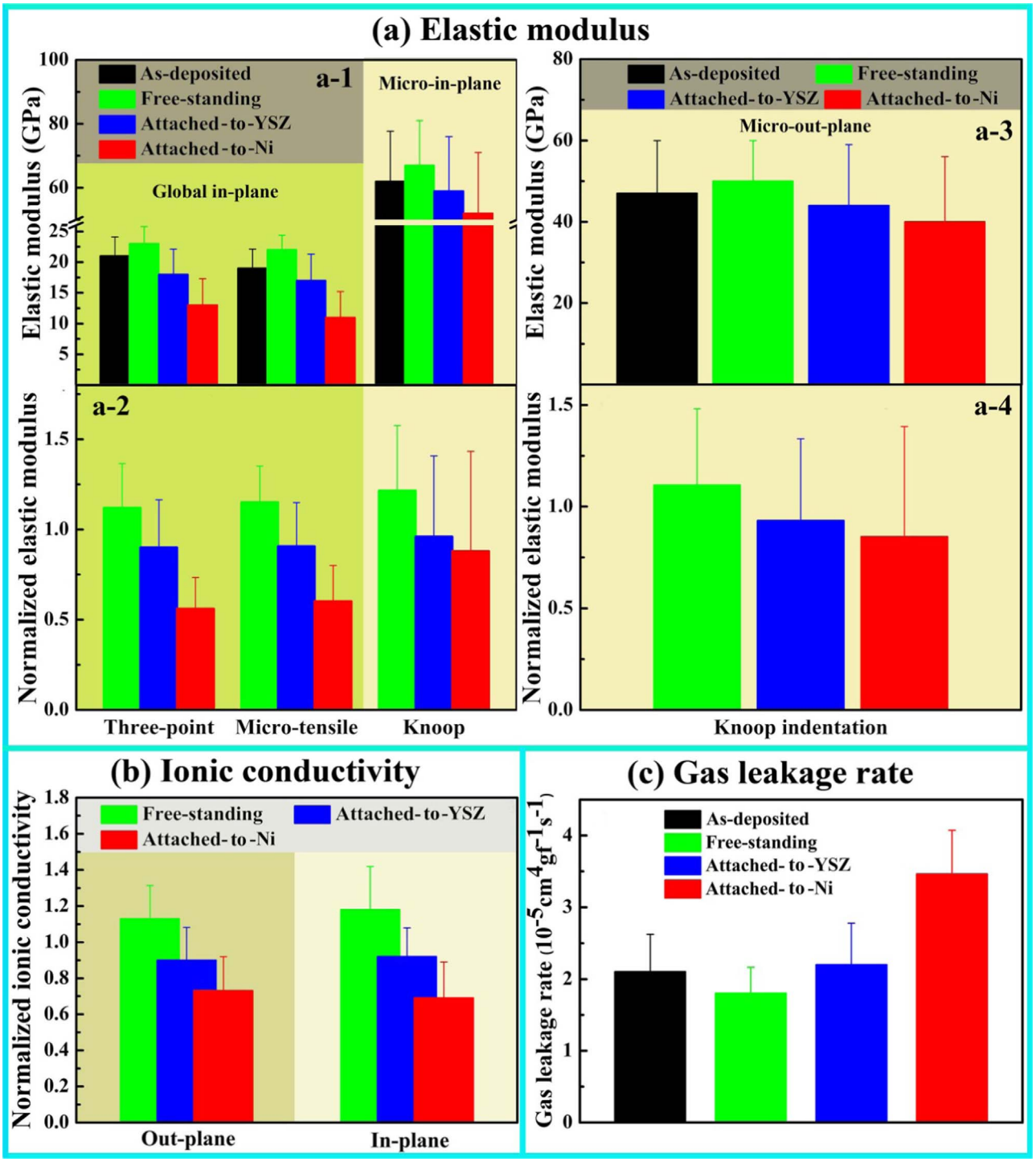

Fig. 3. Evolution of coating properties after heating: (a) elastic modulus: (a-1) shows the macroscopic and microscopic elastic moduli in the in-plane direction, (a-2) shows the normalized elastic modulus with respect to that in the as-deposited state in the in-plane direction, (a-3) shows the microscopic elastic modulus in the out-plane direction, (a-4) shows the normalized elastic modulus with respect to that in the as-deposited state in the out-plane direction. (b) Normalized ionic conductivity with respect to that in the as-deposited state at 800 °C in the in-plane and out-plane directions and (c) gas leakage rate.

cannot be measured with precision using the widely employed laser flash method. Given the similarity between the properties of thermal conductivity and electric conductivity and their analogous nature, in this study, we measured the ionic conductivities of the YSZ coatings. Fig. 3b shows the changes in the ionic conductivities of the YSZ coatings after heating. It can be seen that heating led to changes in the ionic conductivities of the different coatings that were similar to those induced in the mechanical properties, as shown in Fig. 3a. The ionic conductivity of the free-standing coatings increased slightly after heating while that of the Attached-to-YSZ coatings decreased slightly. Further, the Attached-to-Ni coatings showed a marked decrease in ionic conductivity upon heating. Moreover, for all the coatings, the changes in ionic conductivity in the in-plane direction was comparable to that in the out-plane direction after heating. The ionic conductivity in both directions is reflective of the coating structure in a relatively macroscale perspective. The ionic conductivity is dependent with the lamellar structure with a connected 2D pore network [50,51].

The APS ceramic coating often presents a poor gas tightness due to

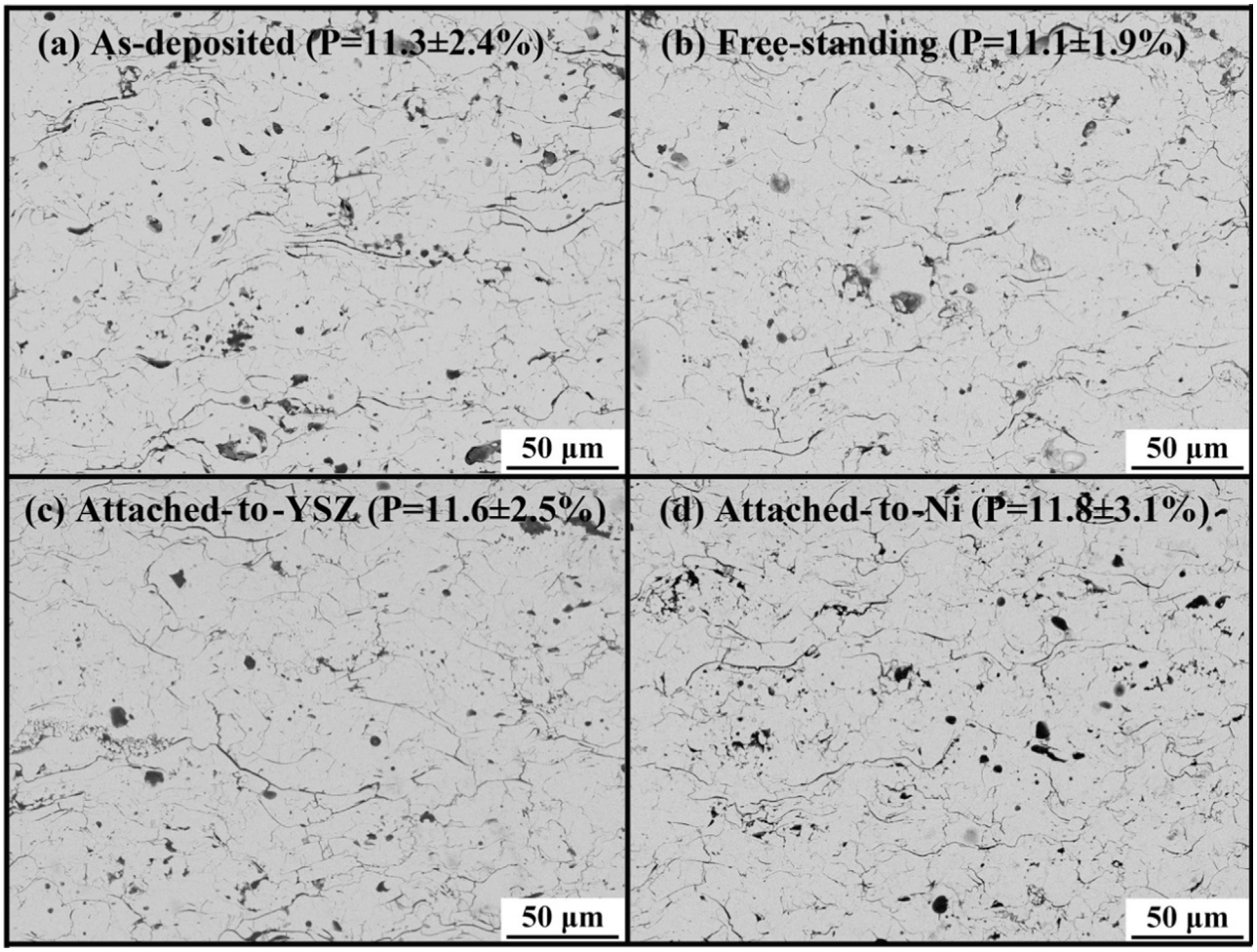

Fig. 4. Evolution of the microstructure of APS YSZ coatings and their apparent porosity in different states: (a) As-deposited, (b) Free-standing, (c) Attached-to-YSZ, and (d) Attached-to-Ni.

its connected 2D pore network [53,54]. Fig. 3c shows the changes in the gas leakage rates of the YSZ coatings after heating. It can be seen that the gas leakage rates of the free-standing and Attached-to-YSZ coatings were almost comparable to those in the as-deposited state. However, after heating, the Attached-to-Ni coatings showed a gas leakage rate nearly twice as large as that in the as-deposited state, suggesting that the structural changes induced in them had enhanced pore connectivity.

To sum up, the heating-induced changes in properties of the YSZ coatings attached to substrate indicated that the as-deposited structure is further changed. Moreover, the combined-effect of the residual stress and the CTE mismatch strain enhances the structural changes upon heating.

3.2. Evolution of microstructure from a macroscale perspective

Fig. 4 shows the macroscale structure of the various YSZ coatings after heating. It can be seen that the YSZ coatings exhibited a distinct lamellar structure consisting of a network of connected pores. After heating, there was no obvious structural change in the coatings even for the case of the Attached-to-Ni coatings. The apparent porosities of the coatings also confirmed this phenomenon. It is believed that the APS YSZ coatings exhibit excellent strain tolerance owing to a large amount of the 2D pores [8,21]. Accordingly, there were no macrosclae cracks induced upon heating. It was necessary to account for the above-described changes induced in the properties of the coatings from a microscale perspective.

4. Discussion

4.1. Structural evolution from a microscale perspective

The PS-YSZ coatings have a lamellar structure that consists of a connected network of inter/intrasplat pores [11,12]. Upon heating, the residual stress and the CTE mismatch strain work as the driving force to induce structural changes. The large numbers of intersplat pores and intrasplat cracks act as defect sources and expand under the CTE mismatch strain. Fig. 5 shows the strain-induced expansion at the microscale pore tips in the individual splats and coatings after heating. Owing to the fact that the individual splat segments are the basic units constituting a coating, the structural changes induced in the individual splats are discussed first, as shown in Fig. 5(a and b). To begin with, from the images of the individual splat surfaces, it can be seen that the cracks widened after heating irrespective of the substrate material used. The widening degree of the intrasplat cracks was relatively smaller for the YSZ substrates than that for the magnesia substrates. Secondly, from the images of the interfaces formed between the individual splats and substrates, it was observed that partial but distinct interfacial tearing occurred after heating in the case of the Attached-to-magnesia splats. In the case of the Attached-to-YSZ splats, the degree of interfacial tearing was not as significant. Similarly, strain-induced interlamellar tearing and the formation of new cracks inside layers were observed in the Attached-to-Ni coatings, as shown in Fig. 5c. In brief, these structural changes based on the individual extension of the preexisting intersplat pores and intrasplat cracks can be called microscale structural changes.

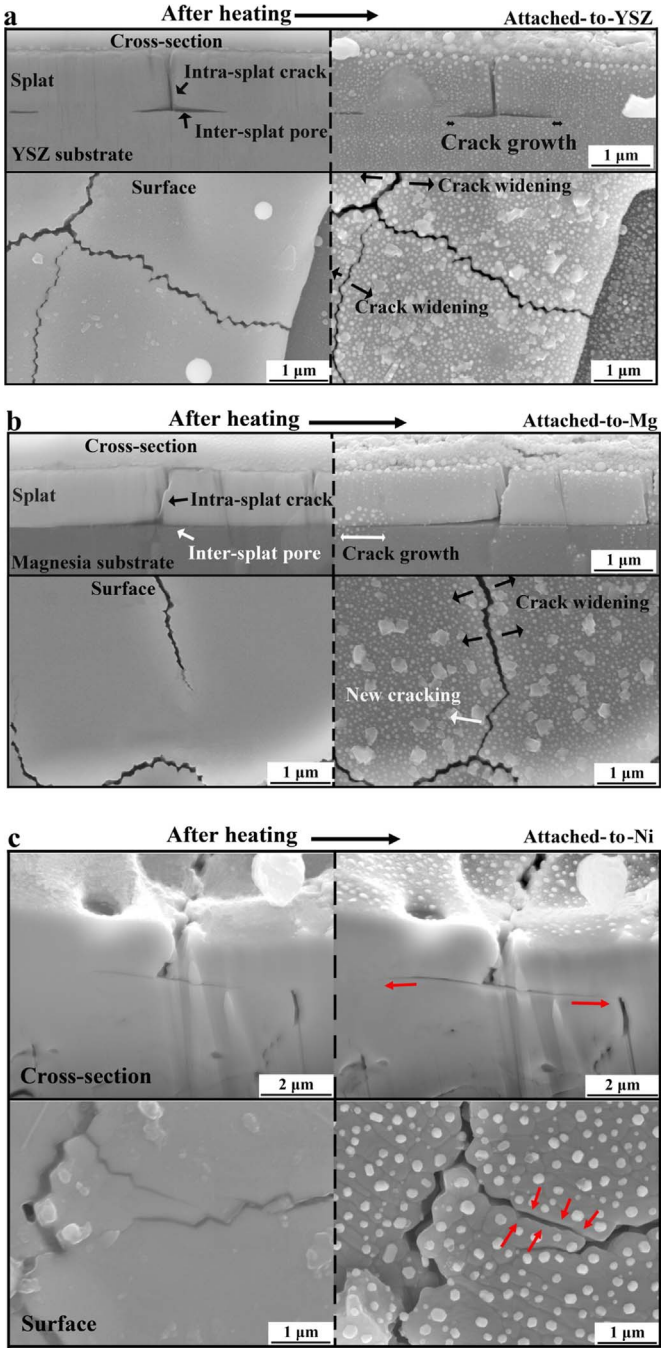

Fig. 5. Strain-induced microscale pore tips extending in individual YSZ splats and YSZ coatings after heating: (a) individual splats attached to a YSZ substrate; (b) individual splats attached to a magnesia substrate, and (c) YSZ coatings attached to a Ni-based superalloy substrate.

To sum up, the expansion of the 2D pores, which included intersplat tearing and intrasplat cracking, is the main microscopic structural change induced in the coatings by strain. The quantity of intersplat pores is strongly related to the bonding ratio of the coatings. Therefore, the changes in the 2D pore length density and the bonding ratio were determined to statistically analyze the structural evolution, as shown in Fig. 6. The post-heating length density of the intersplat pores of the free-standing coatings was comparable to that in the as-deposited state. In contrast, the Attached-to-YSZ coatings showed a slight increase as compared to that in the as-deposited state. This increase was more pronounced in the case of the Attached-to-Ni coatings. In the case of the intrasplat cracks, the free-standing and Attached-to-YSZ coatings exhibited the same density value after heating as was the case in the as-deposited state. The Attached-to-Ni coatings exhibited a slightly higher length density of intrasplat cracks, in contrast. However, the increase in length density of intrasplat cracks was relatively smaller than that in the intersplat pores, as shown in Fig. 6b. There were two reasons for this phenomenon. The first was related to the different morphologies of intersplat pores and intrasplat cracks. Owing to the limited bonding area between layers, the intersplat pores separate the neighboring layers partially [10–12]. However, the intrasplat cracks are generated during quenching stage after liquid splat drops compacting on the substrate [21]. To release to quenching stress, most intrasplat cracks run through the thickness of a splat. Consequently, the intersplat pores separate the neighboring two layers partially, whereas the intrasplat cracks separate the splat totally [12]. Based on the analysis described above, the number of intersplat pore tips is much higher than that of intrasplat crack tips. Upon heating, the strain-induced extension of the 2D pores occurs primarily along the pore tips. The fact of a larger number of intersplat pore tips results in a greater increase in the length density of intersplat pores. The second is that the intersplat tearing usually occurs prior to intrasplat cracking. This is highly related to the unique structure of plasma sprayed YSZ coatings. As mentioned above, the intersplat pores separate the neighboring layers partially, whereas the intrasplat cracks often separate the splat segments completely in one layer. Therefore, the limited bonding areas between layers are the primary skeleton to connect neighboring layers. Moreover, the limited bonding areas would be the dominant carriers to transmit load from layer to layer. Actually, the stress is firstly transmitted from substrate to the first layer of the coating. Following on, the stress is further transmitted layer-by-layer until the top layer of the coating. It is reported that the force transmission between coating and substrate is shear-dominant [55,56]. This condition is also applicable to the layer structure. Therefore, shear stress is transmitted from the substrate to the coating in a layer-by-layer manner. The limited bonding areas between the various layers are where the shear stress is transmitted. Consequently, partially intertearing in the bonding area occurs firstly. This is consistent with the results of analytical studies [34], namely, that under shear stress, the extension of intersplat pores occurs more readily than their nucleation. After the intertearing, the residual bonding areas probably act as skeletons and transmit stress to the upper layer, leading to the propagation of the preexisted intrasplat cracks in the upper layer. In brief, for every layer, the shear stress is firstly applied on its limited bonding areas. Subsequently, this stress can be transmitted into the upper layer. Therefore, the intersplat tearing is often prior to intracracking based on the force transmission mechanism in the unique layer structure.

Based on the analysis described above, the microscale structural changes including intersplat tearing and intrasplat cracking are essentially responsible for the changes seen in the microscale elastic modulus (Fig. 3a). The Knoop indenter usually covers a length of approximately 70–100 μm along its long axis [49]. This length would be equal to the combined length of several splat segments. Therefore, the microscale elastic moduli determined using the Knoop indentation tests were actually reflective of the strain tolerance of several splat segments. Consequently, from a microscale perspective, it can be concluded that the phenomena of intersplat tearing and intrasplat cracking resulted in a slight decrease in the elastic modulus in the case of the Attached-to-Ni coatings. However, the decrease in the macroscale properties was much larger than that in the microscale properties, suggesting that some other larger-scale structural changes are also induced by the strain.

4.2. Formation of mesoscale cracks

It is widely believed that the structure of APS ceramic coatings is nonuniform and intricate [10,17], suggesting that the bonding ratio

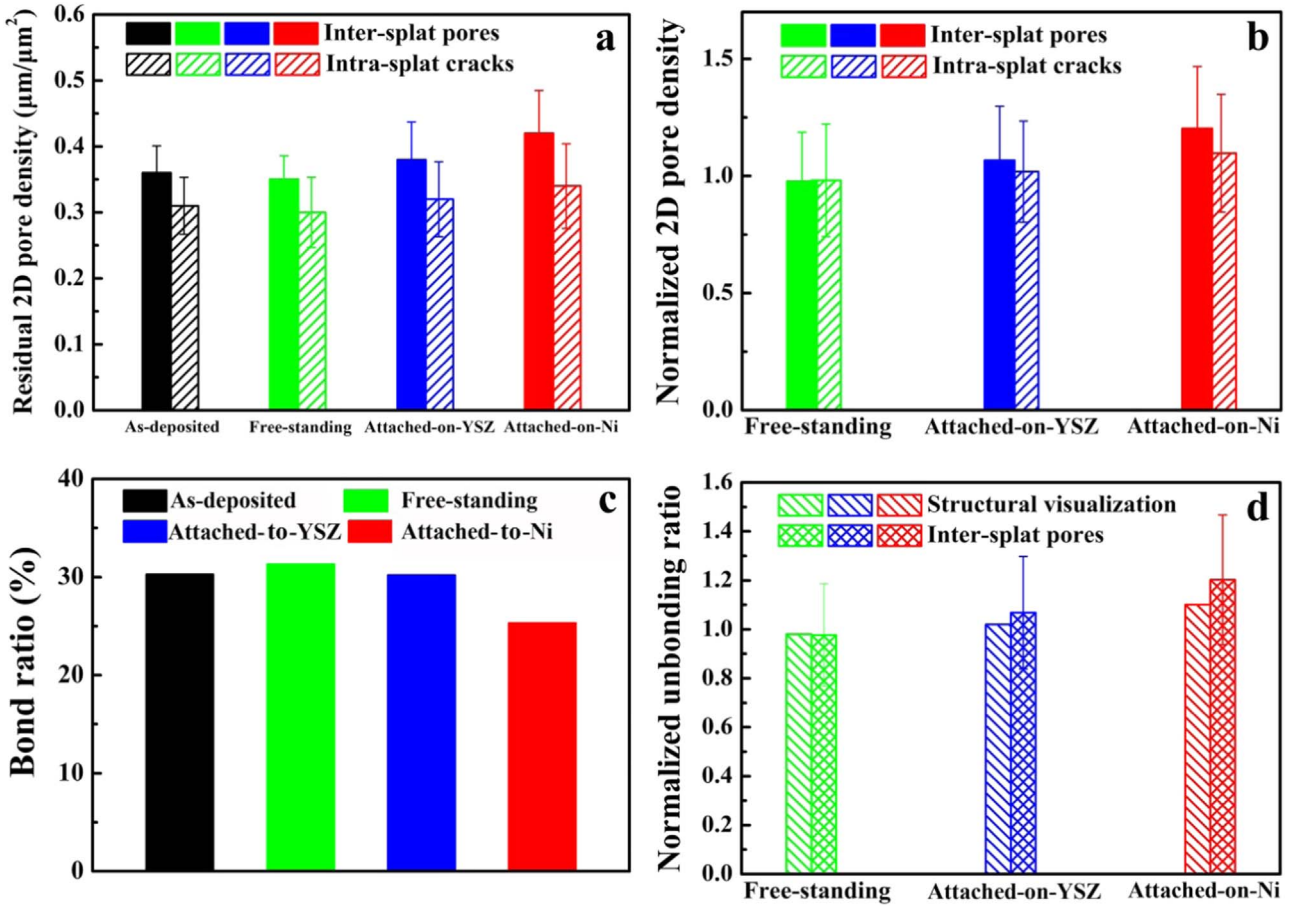

Fig. 6. Evolution of microstructure of YSZ coatings after heating, based on statistical data: (a) 2D pore length density, (b) normalized 2D pore density with respect to that in the as-deposited state, (c) apparent bonding ratio obtained from structural visualization, and (d) normalized unbonding ratio with respect to that in the as-deposited state, as determined by structural visualization and based on the intersplat pore length density.

between the various layers probably varies around the mean value from segment to segment. In larger bonding areas, partially interlamellar tearing occurs. The residual area then transmits the stress further. In smaller bonding areas, the interlamellar tearing is complete. These region-sensitive structural changes are probably strongly related to the changes in the macroscale properties.

Fig. 7 shows two kinds of strain-induced large cracks formed when several intrasplat cracks in neighboring layers connect. The first type of cracks is related to totally intersplat tearing in smaller bonding areas, as shown in Fig. 7a. The existing intrasplat cracks in the neighboring layers connect together in this case. The second type of cracks is related to the partially interlamellar tearing that accompanies the extension of the intrasplat cracks in the larger bonding areas, as shown in Fig. 7b. The intrasplat cracks extend and connect with the intersplat pores. In

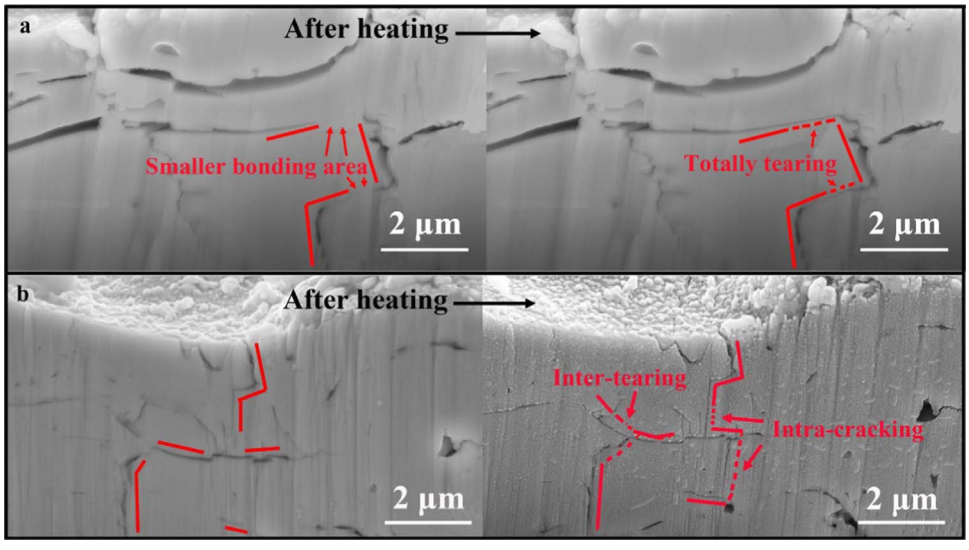

Fig. 7. Mesoscale cracks induced by (a) totally interlamellar tearing in the smaller bonding area and (b) intrasplat cracking accompanied by partially interlamellar tearing in the larger bonding area.

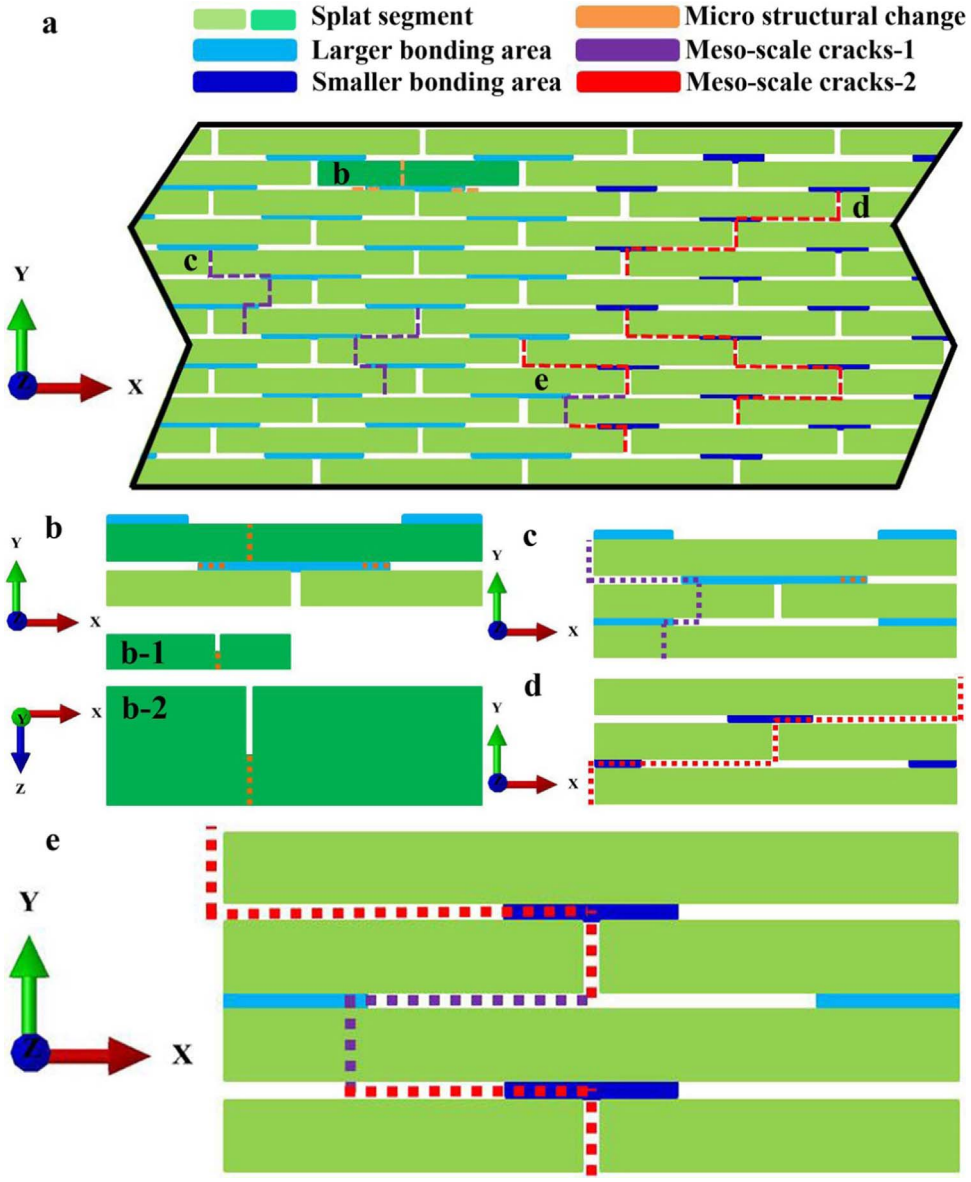

Fig. 8. Schematic diagram of the actual starting state before sintering based on the strain-induced structural changes after heating: (a) macroscopic view of the strain-induced structural changes, (b) typical microstructural changes, including intersplat tearing and intrasplat cracking, and (c) mesoscale crack-1 induced by intrasplat cracking and partially intersplat tearing in a region with a higher bonding ratio, (d) mesoscale crack-2 induced by totally intersplat tearing in a region with a lower bonding ratio, and (e) a mesoscale crack formed by both the mechanisms (i.e., those corresponding to (c) and (d)).

this region, the residual bonding areas still act as carriers to transmit stress to the segments. These two kinds of extensions both lead to several of the existing cracks connecting with each other, resulting in cracks that are relatively larger than the microscale inter/intrasplat pores. Owing to the excellent strain tolerance of APS YSZ coatings [8,12,21], these cracks cannot extend further and form macroscale cracks. This is the reason no obvious change was observed in the Attached-to-Ni coatings after heating from a macroscale perspective (see Fig. 4). Therefore, these two kinds of cracks can be called mesoscale cracks. In actual coatings, a few mesoscale cracks may also be formed by these two mechanisms acting in combination. In brief, these coherent structural changes based on the connection of several inter/intrasplat defects can be called mesoscale structural changes.

4.3. Effect of mesoscale cracks on properties

The mesoscale cracks generated in some regions can be attributed to the nonuniform structure of APS coatings. The formation of mesoscale cracks makes the coatings even more nonuniform. The microscale and mesoscale structural changes contribute significantly to the strain tolerance and are responsible for approximately 50% of the drop in the macroscopic elastic modulus in the in-plane direction, as shown in Fig. 3a. These multiscale structural changes also affect the service lifetime of TBCs, since they enhance the strain tolerance. Enhancing the strain tolerance of TBCs by tailoring their structure has been the focus of many studies. For instance, a few researchers [57,58] have designed macroscale dense vertical cracks (DVCs) in as-deposited coatings to ensure a higher macroscale strain tolerance, which usually results in a higher thermal cycling life. However, when such DVCs are formed, the coatings often exhibit a partially dense structure between the cracks, which presents deteriorative effect on thermal insulation. The results of this study suggest that forming mesoscale cracks may be an alternative method of decreasing the macroscale elastic modulus significantly without adversely affecting the partial thermal barrier performance. Mesoscale cracks would be much smaller than the DVCs formed in the above-mentioned study.

Moreover, the strain tolerance of TBCs in the as-deposited state would prevent these mesoscale cracks from expanding into large-scale cracks. In other words, the increase in the strain tolerance induced by large DVCs may also be realized by forming uniformly distributed mesoscale cracks in the as-deposited porous structure.

The macroscale ionic conductivity and elastic modulus in the in-plane direction both decreased after heating. However, the extent of decrease in the ionic conductivity was smaller than the decrease in the elastic modulus. The reason for this is related to the unique structure of APS YSZ coatings. It has been shown that the ionic conductivity in the out-plane direction is dependent on the bonding areas [50,59]. In fact, the bonding areas also act to transmit ions in the in-plane direction dominantly, owing to the fact that most intrasplat cracks run through the thickness of the splat [11,12]. This means that it is relatively difficult to conduct ions through single layer owing to the most separated splat segments. Therefore, the decrease extent of the ionic conductivity in the in-plane direction was comparable to that in the out-plane direction. Given the fact that most mesoscale cracks are generated by the connecting of existing cracks, the drop in the ionic conductivity can primarily be attributed to the phenomena of inter-lamellar tearing and intrasplat cracking. Therefore, the effect of the mesoscale cracks on the ionic conductivity is actually similar to that of the microscale structural changes. In other words, regardless of whether the microscale intersplat tearing is totally or partially, the ionic conductivity depends on the 2D pore length density. The unbonding ratio of the Attached-to-Ni coatings was approximately 110–120% of that in the as-deposited state (see Fig. 6d). Consequently, the change in the ionic conductivity was approximately 15–20% as estimated using the model developed by Xing et al. [59]. This is just a little smaller than the experimental results, owing to the fact that the new intrasplat cracks were not taken into consideration.

However, the elastic modulus is usually much more sensitive to its corresponding vertical cracks [60]. Therefore, in addition to being affected by the microscale structural changes, the macroscale elastic modulus in the in-plane direction is also significantly affected by the mesoscale cracks, since they would be oriented vertically with respect to the coating surface. Consequently, a large number of mesoscale cracks in coatings should lead to a greater drop in the macroscale elastic modulus compared to that in the ionic conductivity.

4.4. Actual starting state prior to sintering

The experimental data obtained in this study and the discussion presented above confirm that multiscale structural changes occur in TBCs upon heating. The limited bonding areas are the primary carriers to transmit stress from substrate to layers. The bonding area is dominantly stressed by shear stress, while the splat segment is loaded primarily by normal stress. Fig. 8 shows a schematic diagram of these strain-induced multiscale structural changes. The basic structural change is the extension of microscale 2D pores, as shown in Fig. 8b. For the formation of mesoscale cracks in the region with larger bonding areas, partially interlamellar tearing occurs. Consequently, the residual bonding areas still transfer stress to the splat segments, leading to further intrasplat cracking. These new cracks can connect with the existing cracks in the neighboring layers, resulting in the formation of a few relatively larger cracks (labeled as mesoscale cracks-1 in this study), as shown in Fig. 8c. In the region with smaller bonding areas, the interlamellar tearing is complete, resulting in the formation of mesoscale cracks-2, as shown in Fig. 8d. Obviously, a few mesoscale cracks may also appear through the combination the two aforementioned types of cracks, as shown in Fig. 8e.

As described in the Introduction, most studies on thermally exposed PS-YSZ coatings have been based on free-standing coatings, meaning that the as-deposited state of the coatings is treated as their starting state before sintering. However, in this study, we observed distinct multiscale structural changes induced by strain upon heating. Accordingly, the actual starting state prior to sintering of the coatings attached to substrates is different from the as-deposited state. There is no doubt that the starting state of PS-YSZ coatings significantly affects their sintering behavior [18,19]. The strain-induced structural changes result in the generation of even more pores, thus decreasing the macroscale elastic modulus significantly. The enhanced strain tolerance may have a positive effect on the durability of TBCs. Therefore, by determining the actual starting state prior to sintering, the actual evolution of the structure and properties of constrained coatings during thermal exposure may be investigated.

5. Model development

5.1. Modification on developed structural model

The experimental part described multiscale structural changes induced by extra strain. The resulted structure presented an even lower elastic modulus with respect to the as-deposited state (see Fig. 3). Consequently, contradicted to initial perception, the strain-induced multiscale damage on the porous structure would present a positive effect on the thermal cyclic lifetime of TBCs. In this section, we describe the effects of the strain-induced multiscale structural changes on the elastic modulus using a structural model. As discussed in Section 4.2, the pore tip number of intrasplat crack is much smaller than that of intersplat pores. Moreover, intersplat tearing occurs prior to intrasplat cracking. Consequently, intersplat tearing, either total or partial, would be the primary structural change induced under strain.

Fig. 9 shows the development of a structural model based on lamellar YSZ coatings. Based on a previous study [12], the basic unit of a PS-YSZ coating was considered a splat segment divided by intrasplat cracks. The following assumptions were made when developing the model: (i) all the splat segments of various shapes and sizes were assumed to be cubic and having the same length and thickness; these were considered the structural units; (ii) the partially bonded area was assumed to be located at the bottom center of the structural units; (iii) the intrasplat crack tips were neglected, leaving only the totally separated segments in each layer; (iv) the structural units were assumed to be stacked on the lower layer uniformly, meaning that every structural unit was uniformly located at the region consisting of the four corners of the four structural units in the lower layer, as shown in Fig. 9(a-2 and a-3). The developed model was symmetrical. The representative structural patterns for multilayer stacking are shown in Fig. 9(a-4 and a-5). In detail, the representative structural pattern, termed as a calculating unit, presents a structural unit bonded to four quarters belonging to the structural units in the lower layers. A periodic boundary condition was used with the corresponding-pair surfaces (see the pink and blue regions in Fig. 9(a-5)), with the aim of ensuring a same strain behavior under stress. The procedure for applying the periodic boundary conditions has been described elsewhere [61].

In the case of the microscale structural changes induced by partially intersplat tearing, the calculations for the elastic modulus were based on the basic unit, as shown in Fig. 9(a-4). In the case of the mesoscale cracks induced by totally intersplat tearing, the calculating unit was formed by extending the basic unit to one consisting of n basic units in the x-z plane and 10 layers stacked along the y-axis, as show in Fig. 9b. Totally intersplat tearing would occur at the bonding areas located at the edges of the basic units. In this study, it was assumed that a single totally intersplat tear meant that the tearing process induced connections of the intrasplat cracks in two neighboring layers. An example is shown in Fig. 9(b-3), wherein two totally intersplat tears occur (red dotted lines) to form a mesoscale crack (shown by black dotted lines) by inducing connections of the intrasplat cracks in three neighboring layers. Periodic boundary conditions were also used for the corresponding-pair surfaces of the n-extended unit.

Based on the model described above, the micro- and mesoscale structural changes could be investigated. The microstructural changes

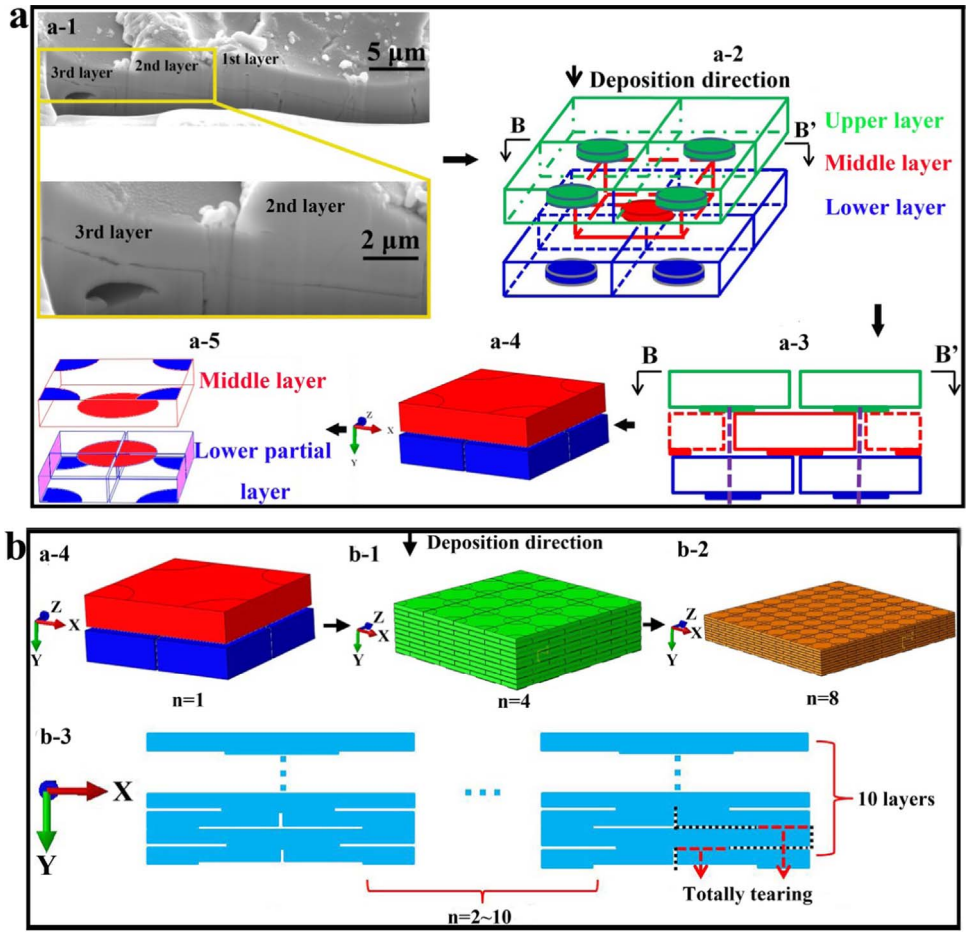

Fig. 9. Developed structural model based on lamellar YSZ coatings: (a) the developed basic model with multilayer stacking. In detail, (a-1) is the cross-section of a YSZ coating, (a-2) is the developed structural model corresponding to (a-1), (a-3) is the cross-section corresponding to (a-2), (a-4) is a simplified periodic pattern corresponding to the purple dotted lines in (a-3) and is termed as a basic unit, and (a-5) is a separated pattern of (a-4) presenting the bonding conditions between the layers. (b) Modified structural model based on a basic unit to *n*-extended unit with *n* basic units perpendicular to the deposition direction and 10 layers stacked along the deposition direction. In detail, (b-1) is an extended unit with n=4, (b-2) is an extended unit with n=8, and (b-3) is a schematic diagram of intersplat tearing that occurs on the extended units.

affected the elastic modulus by changing the bonding ratio of the basic units, as shown in Fig. 9(a-4). For the mesoscale cracks related to the *n*-extended unit, the magnitude of the cracks along the deposition direction was determined by the number of totally interlamellar tears. Here, *n* stands for the number of basic units between mesoscale cracks, meaning that a mesoscale crack appeared at every *n* basic units perpendicular to the deposition direction. Therefore, the modified model allowed us to investigate the effects of the magnitude of the cracks along the y-axis and the crack number density along x-axis on the elastic modulus.

The numerical simulations were performed using the commercial FEM code ABAQUS. To calculate the elastic modulus in the in-plane direction, a strain was applied to the cross-sections of the partial layers along the x-axis. Consequently, the elastic modulus of the structure could be obtained from the stress-strain curve [12]. Herein, the structural units were assumed to be homogeneous, isotropic, and linear elastic. The Young's modulus and Poisson's ratio of bulk YSZ were taken to be 205 GPa and 0.23, respectively [38]. All the bonds between the structural units were realized using Tie constraints. Meshing was performed with 0.2 μm global seeds using the Tet element shape. The other details to obtain elastic modulus can be found elsewhere [12].

5.2. Effects of microstructural changes on elastic modulus of structural model

The structural parameters for a basic unit, namely the length, thickness and bonding area, have significant effect on the elastic modulus of the whole structure. As reported previously [12], the elastic modulus often vary linearly with length and thickness in in-plane direction. In actual coatings, the length and thickness of splat segments are distributed in certain ranges. Therefore, it is reasonable to choose mean values of the length and thickness for numerical calculation. Similar to the previous study [12], this study obtained the statistical segment length and thickness from coating surface and polished cross-section, respectively. The length of segments distributes in a range of 6–15 μm, while the thickness is 0.8–1.5 μm. Consequently, the mean values of the length and thickness used in this study is chosen to be 10 μm and 1 μm, respectively.

In the case of microscopic structural changes, partially intersplat tearing leads to a decrease in the bonding ratio between layers. Fig. 10 shows the effect of the bonding ratio on the elastic modulus in the in-plane direction. As shown in Fig. 6, the initial bonding ratio obtained from the structural visualization was approximately 30%. After heating, the bonding ratio decreased to approximately 22–26%. The normalized elastic modulus with initial state after heating is inserted in Fig. 10. It can be seen that the elastic modulus decreased by approximately 10–15% owing to the microstructural changes. On the one hand, this was in keeping with the results of the Knoop indentation tests, as shown in

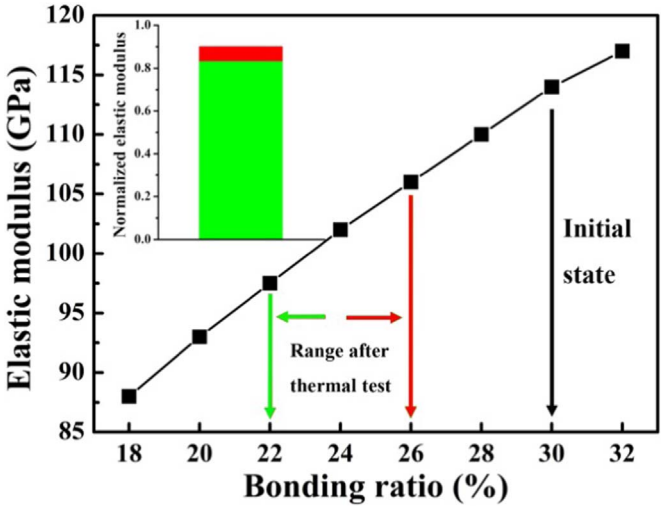

Fig. 10. Effects of the bonding ratio on the elastic modulus in the in-plane direction. The inset figure shows the normalized elastic modulus after heating with respect to that in the initial state.

Fig. 3a. On the other hand, the drop was much smaller than that on the macroscale, further confirming the fact that microscale changes are not large enough to decrease the macroscale elastic modulus by 50%.

5.3. Effect of mesoscale cracks on elastic modulus

Owing to the symmetry of the developed model, two distinct bonding ratios were chosen to simulate the variations in the bonding ratio in actual coatings. Fig. 11 shows the effect of the number density of the mesoscale cracks induced by a single totally intersplat tear on the elastic modulus. To begin with, a common phenomenon observed for the two different bonding ratios was that the drop in the elastic modulus increased dramatically in the case of the less-assembled basic units (n=2–5), meaning that a higher number density of mesoscale cracks along the x-z plane had a greater effect on the strain tolerance. Therefore, it was reasonable to choose the largest *n* as 10, in order to investigate the effects of the number density of the mesoscale cracks on the macroscale elastic modulus. Secondly, a lower bonding ratio resulted in a larger decrease in the elastic modulus. Given that the experimental data showed that totally intersplat tearing is more likely to occur in regions with smaller bonding areas, the macroscale elastic modulus would be significantly affected by the strain-induced mesoscale cracks.

The above-described data show the preliminary effects of the number density of the mesoscale cracks corresponding to a single tear on the macroscale elastic modulus. However, a single totally intersplat tear can also increase the tearing possibility of the bonding area in the neighboring layers. Fig. 12 shows the evolution of the shear stress distribution after tearing occurred in a neighboring layer. It can be seen that the shear stress in the bonding area in one of the layers is significantly higher owing to the tearing of the bonding area in a neighboring layer, as shown in Fig. 12b. This means that the occurrence of a single tear increases the probability of another tear occurring in the neighboring layers. Consequently, mesoscale cracks often cover more than two layers. When another tear occurs, the shear stress decreases markedly, as shown in Fig. 12c. Consequently, the mesoscale cracks induced by multiple tears often cover the limit layers with several tears. This suggests that the size of the mesoscale cracks is often not too large.

Fig. 13 shows the effects of the multiple-tears-induced mesoscale cracks on the elastic modulus. When the number of totally intersplat tears increased along the deposition direction, the elastic modulus decreased dramatically, as shown in Fig. 13(a, b). Despite the bonding ratios, the less-assembled basic units (n=2–5) showed an even sharper drop in the elastic modulus with the increase in the number of tears along the deposition direction. Moreover, the less-assembled basic units exhibited a 50% decrease in the elastic modulus when fewer tears were formed. For example, 2 assembled basic units (n=2) would require 4 totally intersplat tears in the neighboring layers for a bonding ratio of 28%. Similarly, for n=3, 6 totally intersplat tears would be needed; and for n=5, 8 totally interlamellar tears would be needed. This phenomenon is similar to that in the case of a smaller bonding ratio (18%), which would require even fewer tears for the elastic modulus to drop by half. Similar to the trend seen in the case of a single tear in Fig. 11, the elastic modulus was more sensitive to the mesoscale cracks corresponding to fewer assembled basic units (n=2–5). When n was larger than 6, the decrease in the elastic modulus was not so obvious; this was the case even for a greater number of tears in the out-plane direction, as shown in Fig. 13c, which displays the normalized elastic modulus.

To summarize, mesoscale cracks have a significant effect on the macroscale elastic modulus of TBCs. Moreover, a lower bonding ratio is more sensitive to the totally intersplat tearing induced drop in the elastic modulus. Secondly, both the crack number density in the in-plane direction and the size in the out-plane direction affect the elastic modulus. To induce a similar decrease in the elastic modulus, a higher number density would be needed in the case of smaller mesoscale cracks. Thirdly, when smaller mesoscale cracks are present in a higher

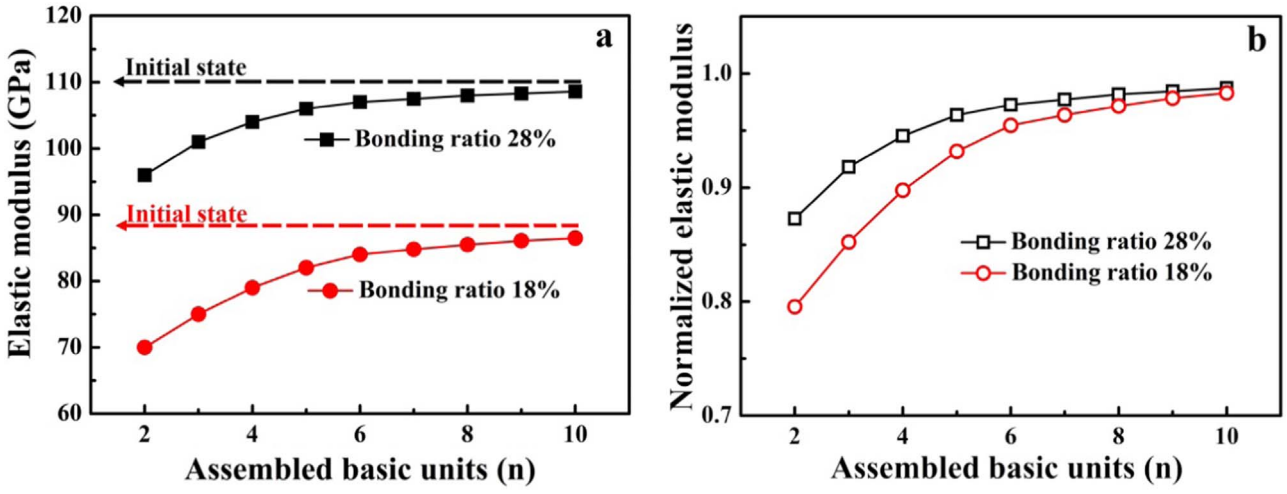

Fig. 11. Effects of the number density of single-tear-induced mesoscale cracks on elastic modulus: (a) effect of a single tear with assembled basic units and (b) normalized elastic modulus with respect to that in the initial state corresponding to (a).

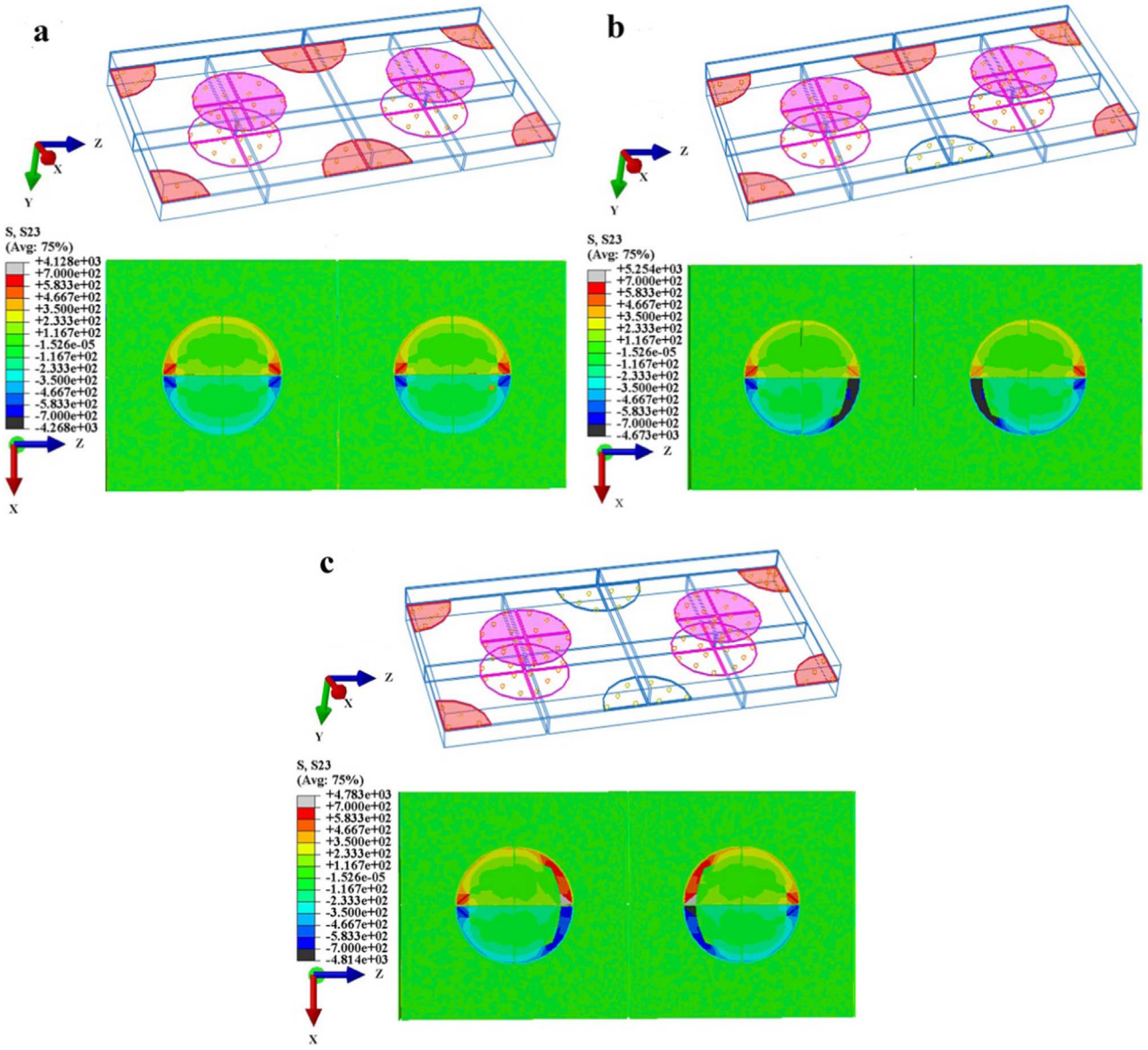

Fig. 12. Evolution of the shear stress distribution after occurrence of tearing in a neighboring layer with half of the 2-basic-units-assembled structure. (a) initial state, (b) after occurrence of tearing in half of the bonding area, and (c) after occurrence of tearing in the entire bonding area.

number density, the strain tolerance is higher compared to that for larger cracks present in a lower number density. For example, 4-tears-induced mesoscale cracks in a 3-basic-units-assembled structure lead to a greater drop in the elastic modulus compared to that in the case of 8-tears-induced mesoscale cracks in a 10-basic-units-assembled structure, as shown in Fig. 13b. These results should lead to the development of a novel method for tailoring the structures of TBCs without causing significant damage so that they exhibit higher strain tolerances.

6. Conclusions

In this study, the post-heating strain-induced structural changes in YSZ coatings attached to substrates with different CTEs were investigated. The multiscale structural changes resulted in scale-sensitive properties changes. A general structural model was developed to investigate the effects of the multiscale structural changes on the mechanical properties from both micro- and macroscale perspectives. The conclusions of the study are as follows:

(i) In keeping with the microscale structural changes resulting from the individual splats, the combined effects of the residual stress and the CTE mismatch strain led to a certain degree of intersplat tearing and intrasplat cracking in the case of the Attached-to-Ni coatings.

(ii) Given the complexity of the structure in the bonding area and the nonuniform scale, a few totally intersplat tears occurred at smaller bonding areas. Meanwhile, a few partially intersplat tears occurred in the larger bonding areas, which were accompanied by an extension of the intrasplat cracks. Both cases led to further connections of the intrasplat cracks in the neighboring layers. Consequently, a few mesoscale cracks covering several layers were formed in the Attached-to-Ni coatings.

(iii) Owing to the multiscale structural changes, the changes in the properties of the Attached-to-Ni coatings were scale-sensitive. The macroscale properties were significantly poorer than those in the as-deposited state, owing to the effects of the micro- and mesoscale structural changes. The microscale properties were more dependent on the microstructural changes and thus exhibited smaller changes as compared to the macroscale properties.

(iv) The developed structural model predicted a drop of approximately

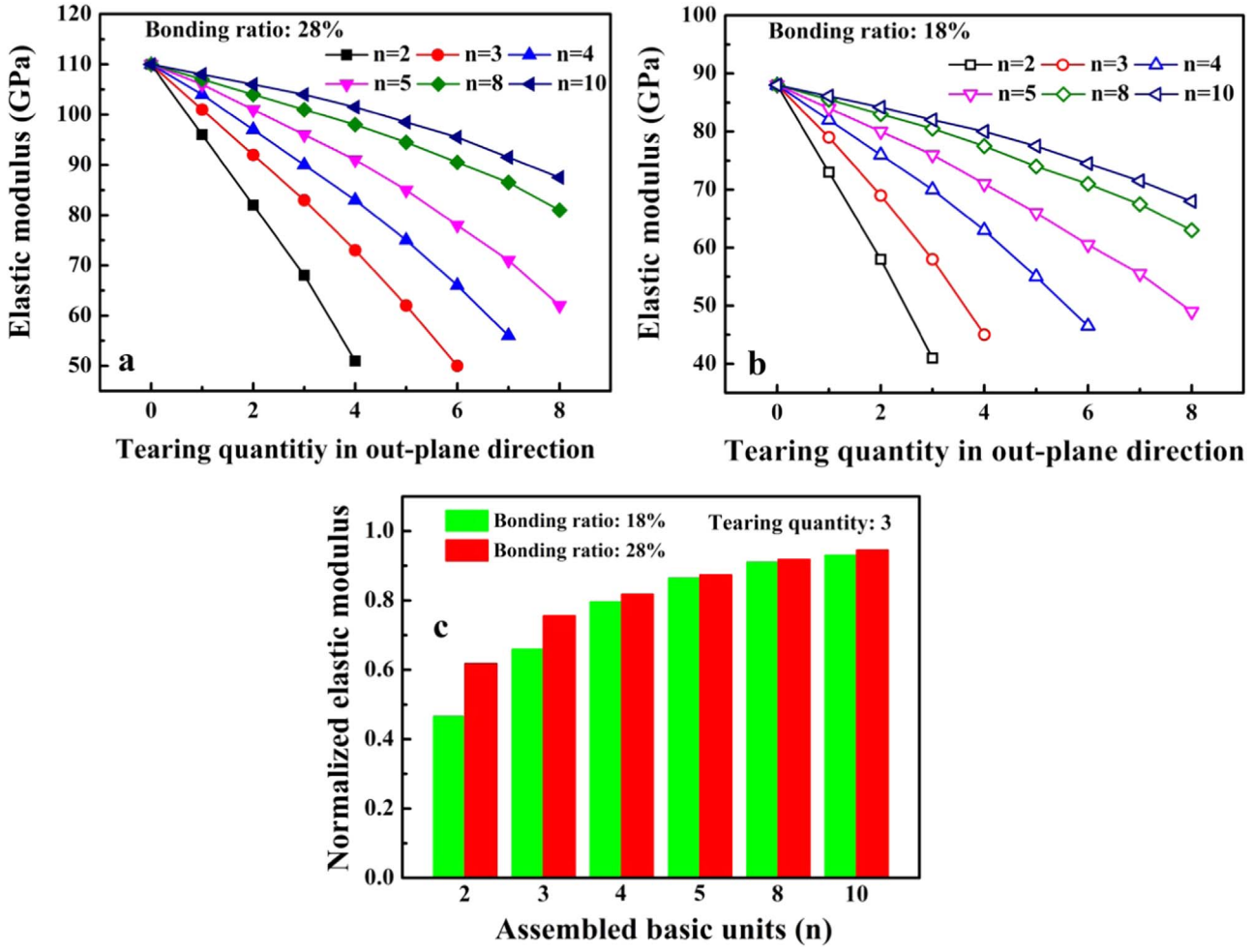

Fig. 13. Effects of multiple-tears-induced mesoscale cracks on the elastic modulus: (a) effect of number of tears on various assembled basic units for a bonding ratio of 28%, (b) effect of number of tears on various assembled basic units for a bonding ratio of 18%, and (c) normalized elastic modulus with respect to that in the initial state varying with the number density in the in-plane direction. The three-tears-induced mesoscale cracks were used to obtain the normalized elastic modulus.

10–15% in the elastic modulus because of the microstructural changes; this was consistent with the elastic modulus values measured by the Knoop indentation test. The intersplat-tearing-induced mesoscale cracks decreased the macroscale elastic modulus significantly. The model also predicted that the crack number density along the in-plane direction and the crack scale along the out-plane direction have significant effects on the macroscale elastic modulus. Furthermore, smaller mesoscale cracks with a higher number density would increase the strain tolerance.

The strain-induced multiscale structural changes observed indicated that the starting state of the coatings before sintering is significantly different from the as-deposited state. Given that the sintering procedure is dependent on the starting structure, determining the actual starting state prior to sintering is essential if one wishes to investigate the actual structural and properties evolution of YSZ coatings attached to substrates during long-term thermal exposure.

Acknowledgments

This project was supported by the National Basic Research Program of China (No. 2013CB035701); the Fundamental Research Funds for the Central Universities; and the National Program for Support of Top-notch Young Professionals.

References

[1] N.P. Padture, M. Gell, E.H. Jordan, Materials science - Thermal barrier coatings for gas-turbine engine applications, Science 296 (2002) 280–284.
[2] R. Vassen, A. Stuke, D. Stover, Recent developments in the field of thermal barrier coatings, J. Therm. Spray. Tech. 18 (2009) 181–186.
[3] C.U. Hardwicke, Y.C. Lau, Advances in thermal spray coatings for gas turbines and energy generation: a review, J. Therm. Spray. Tech. 22 (2013) 564–576.
[4] L. Zhao, Y. Bai, J.J. Tang, K. Liu, C.H. Ding, J.F. Yang, Z.H. Han, Effect of particle in-flight behavior on the composition of thermal barrier coatings, Appl. Surf. Sci. 286 (2013) 184–191.
[5] M. Fevre, A. Finel, R. Caudron, R. Mevrel, Local order and thermal conductivity in yttria-stabilized zirconia. II. Numerical and experimental investigations of thermal conductivity, Phys. Rev. B 72 (2005).
[6] S. Karthikeyan, V. Balasubramanian, R. Rajendran, Developing empirical relationships to estimate porosity and Young's modulus of plasma sprayed YSZ coatings, Appl. Surf. Sci. 296 (2014) 31–46.
[7] Y. Wang, Y. Bai, K. Liu, J.W. Wang, Y.X. Kang, J.R. Li, H.Y. Chen, B.Q. Li, Microstructural evolution of plasma sprayed submicron-/nano-zirconia-based thermal barrier coatings, Appl. Surf. Sci. 363 (2016) 101–112.
[8] Y. Tan, A. Shyam, W.B. Choi, E. Lara-Curzio, S. Sampath, Anisotropic elastic properties of thermal spray coatings determined via resonant ultrasound spectroscopy, Acta Mater. 58 (2010) 5305–5315.
[9] H.J. Ratzer-Scheibe, U. Schulz, The effects of heat treatment and gas atmosphere on the thermal conductivity of APS and EB-PVD PYSZ thermal barrier coatings, Surf. Coat. Tech. 201 (2007) 7880–7888.
[10] C.J. Li, A. Ohmori, Relationships between the microstructure and properties of thermally sprayed deposits, J. Therm. Spray. Tech. 11 (2002) 365–374.
[11] A. Cipitria, I.O. Golosnoy, T.W. Clyne, A sintering model for plasma-sprayed zirconia TBCs. Part I: free-standing coatings, Acta Mater. 57 (2009) 980–992.
[12] G.R. Li, B.W. Lv, G.J. Yang, W.X. Zhang, C.X. Li, C.J. Li, Relationship between lamellar structure and elastic modulus of thermally sprayed thermal barrier coatings with intra-splat cracks, J. Therm. Spray. Tech. 24 (2015) 1355–1367.
[13] P. Fauchais, M. Fukumoto, A. Vardelle, M. Vardelle, Knowledge concerning splat

formation: an invited review, J. Therm. Spray. Tech. 13 (2004) 337–360.
[14] Y. Li, C.J. Li, G.J. Yang, C.X. Li, Relation between microstructure and thermal conductivity of plasma-sprayed 8YSZ coating, Int. J. Mod. Phys. B 24 (2010) 3017–3022.
[15] M. Shinozaki, T.W. Clyne, A methodology, based on sintering-induced stiffening, for prediction of the spallation lifetime of plasma-sprayed coatings, Acta Mater. 61 (2013) 579–588.
[16] S.A. Tsipas, I.O. Golosnoy, R. Damani, T.W. Clyne, The effect of a high thermal gradient on sintering and stiffening in the top coat of a thermal barrier coating system, J. Therm. Spray. Tech. 13 (2004) 370–376.
[17] S. Paul, A. Cipitria, S.A. Tsipas, T.W. Clyne, Sintering characteristics of plasma sprayed zirconia coatings containing different stabilisers, Surf. Coat. Tech. 203 (2009) 1069–1074.
[18] W.G. Chi, S. Sampath, H. Wang, Microstructure-thermal conductivity relationships for plasma-sprayed yttria-stabilized zirconia coatings, J. Am. Ceram. Soc. 91 (2008) 2636–2645.
[19] Y. Tan, J.P. Longtin, S. Sampath, H. Wang, Effect of the starting microstructure on the thermal properties of as-sprayed and thermally exposed plasma-sprayed YSZ coatings, J. Am. Ceram. Soc. 92 (2009) 710–716.
[20] Q. Chen, W.G. Mao, Y.C. Zhou, C. Lu, Effect of Young's modulus evolution on residual stress measurement of thermal barrier coatings by X-ray diffraction, Appl. Surf. Sci. 256 (2010) 7311–7315.
[21] J.A. Thompson, T.W. Clyne, The effect of heat treatment on the stiffness of zirconia top coats in plasma-sprayed TBCs, Acta Mater. 49 (2001) 1565–1575.
[22] S. Guo, Y. Kagawa, Young's moduli of zirconia top-coat and thermally grown oxide in a plasma-sprayed thermal barrier coating system, Scr. Mater. 50 (2004) 1401–1406.
[23] N. Markocsan, P. Nylen, J. Wigren, X.H. Li, A. Tricoire, Effect of thermal aging on microstructure and functional properties of zirconia-base thermal barrier coatings, J. Therm. Spray. Tech. 18 (2009) 201–208.
[24] D.Y. Chen, M. Gell, E.H. Jordan, E. Cao, X.Q. Ma, Thermal stability of air plasma spray and solution precursor plasma spray thermal barrier coatings, J. Am. Ceram. Soc. 90 (2007) 3160–3166.
[25] P.S. Anderson, X. Wang, P. Xiao, Effect of isothermal heat treatment on plasma-sprayed yttria-stabilized zirconia studied by impedance spectroscopy, J. Am. Ceram. Soc. 88 (2005) 324–330.
[26] F. Cernuschi, I.O. Golosnoy, P. Bison, A. Moscatelli, R. Vassen, H.P. Bossmann, S. Capelli, Microstructural characterization of porous thermal barrier coatings by IR gas porosimetry and sintering forecasts, Acta Mater. 61 (2013) 248–262.
[27] F. Cernuschi, P.G. Bison, S. Marinetti, P. Scardi, Thermophysical, mechanical and microstructural characterization of aged free-standing plasma-sprayed zirconia coatings, Acta Mater. 56 (2008) 4477–4488.
[28] R. Dutton, R. Wheeler, K.S. Ravichandran, K. An, Effect of heat treatment on the thermal conductivity of plasma-sprayed thermal barrier coatings, J. Therm. Spray. Tech. 9 (2000) 204–209.
[29] G.J. Yang, Z.L. Chen, C.X. Li, C.J. Li, Microstructural and mechanical property evolutions of plasma-sprayed YSZ coating during high-temperature exposure: comparison study between 8YSZ and 20YSZ, J. Therm. Spray. Tech. 22 (2013) 1294–1302.
[30] J. Moon, H. Choi, H. Kim, C. Lee, The effects of heat treatment on the phase transformation behavior of plasma-sprayed stabilized ZrO_2 coatings, Surf. Coat. Tech. 155 (2002) 1–10.
[31] K.A. Erk, C. Deschaseaux, R.W. Trice, Grain-boundary grooving of plasma-sprayed yttria-stabilized zirconia thermal barrier coatings, J. Am. Ceram. Soc. 89 (2006) 1673–1678.
[32] H. Dong, G.J. Yang, C.X. Li, X.T. Luo, C.J. Li, Effect of TGO thickness on thermal cyclic lifetime and failure mode of plasma- sprayed TBCs, J. Am. Ceram. Soc. 97 (2014) 1226–1232.
[33] B.W. Lv, H. Xie, R. Xu, X.L. Fan, W.X. Zhang, T.J. Wang, Effects of sintering and mixed oxide growth on the interface cracking of air-plasma-sprayed thermal barrier coating system at high temperature, Appl. Surf. Sci. 360 (2016) 461–469.
[34] X.L. Fan, R. Xu, W.X. Zhang, T.J. Wang, Effect of periodic surface cracks on the interfacial fracture of thermal barrier coating system, Appl. Surf. Sci. 258 (2012) 9816–9823.
[35] M. Tillman, J.A. Yeomans, R.A. Dorey, The effect of a constraint on the sintering and stress development in alumina thick films, Ceram. Int. 40 (2014) 9715–9721.
[36] J.S. Kim, R.A. Rudkin, X. Wang, A. Atkinson, Constrained sintering kinetics of 3YSZ films, J. Eur. Ceram. Soc. 31 (2011) 2231–2239.
[37] X. Wang, A. Atkinson, Microstructure evolution in thin zirconia films: experimental observation and modelling, Acta Mater. 59 (2011) 2514–2525.
[38] X.J. Lu, P. Xiao, Constrained sintering of YSZ/Al_2O_3 composite coatings on metal substrates produced from eletrophoretic deposition, J. Eur. Ceram. Soc. 27 (2007) 2613–2621.
[39] A. Cipitria, I.O. Golosnoy, T.W. Clyne, A sintering model for plasma-sprayed zirconia thermal barrier coatings. Part II: Coatings bonded to a rigid substrate, Acta Mater. 57 (2009) 993–1003.
[40] B.R. Marple, R.S. Lima, C. Moreau, S.E. Kruger, L. Xie, M.R. Dorfman, Yttria-stabilized zirconia thermal barriers sprayed using N_2-H_2 and Ar-H_2 plasmas: influence of processing and heat treatment on coating properties, J. Therm. Spray. Tech. 16 (2007) 791–797.
[41] G. Dwivedi, V. Viswanathan, S. Sampath, A. Shyam, E. Lara-Curzio, Fracture toughness of plasma-sprayed thermal barrier ceramics: Influence of processing, microstructure, and thermal aging, J. Am. Ceram. Soc. 97 (2014) 2736–2744.
[42] T.W. Clyne, S.C. Gill, Residual stresses in thermal spray coatings and their effect on interfacial adhesion: a review of recent work, J. Therm. Spray. Tech. 5 (1996) 401–418.
[43] X.C. Zhang, M. Watanabe, S. Kuroda, Effects of processing conditions on the mechanical properties and deformation behaviors of plasma-sprayed thermal barrier coatings: evaluation of residual stresses and mechanical properties of thermal barrier coatings on the basis of in situ curvature measurement under a wide range of spray parameters, Acta Mater. 61 (2013) 1037–1047.
[44] Y. Li, C.J. Li, Q. Zhang, G.J. Yang, C.X. Li, Influence of TGO composition on the thermal shock lifetime of thermal barrier coatings with cold-sprayed MCrAlY bond coat, J. Therm. Spray. Tech. 19 (2010) 168–177.
[45] T. Liu, X.T. Luo, X. Chen, G.J. Yang, C.X. Li, C.J. Li, Morphology and size evolution of interlamellar two-dimensional pores in plasma-sprayed $La_2Zr_2O_7$ coatings during thermal exposure at 1300 °C, J. Therm. Spray. Tech. 24 (2015) 739–748.
[46] C.J. Li, W.Z. Wang, Quantitative characterization of lamellar microstructure of plasma-sprayed ceramic coatings through visualization of void distribution, Mat. Sci. Eng. A-Struct. 386 (2004) 10–19.
[47] T. Zhou, P.L. Nie, H.P. Lv, Q.L. Chen, X. Cai, Assessment of elastic properties of coatings by three-point bending and nanoindentation, J. Coat. Technol. Res. 8 (2011) 355–361.
[48] R.M. Niu, G. Liu, C. Wang, G. Zhang, X.D. Ding, J. Sun, Thickness dependent critical strain in submicron Cu films adherent to polymer substrate, Appl. Phys. Lett. 90 (2007).
[49] R.S. Lima, S.E. Kruger, G. Lamouche, B.R. Marple, Elastic modulus measurements via laser-ultrasonic and Knoop indentation techniques in thermally sprayed coatings, J. Therm. Spray. Tech. 14 (2005) 52–60.
[50] Y.Z. Xing, C.J. Li, C.X. Li, G.J. Yang, Influence of through-lamella grain growth on ionic conductivity of plasma-sprayed yttria-stabilized zirconia as an electrolyte in solid oxide fuel cells, J. Power Sources 176 (2008) 31–38.
[51] C. Zhang, W.Y. Li, H.L. Liao, C.J. Li, C.X. Li, C. Coddet, Microstructure and electrical conductivity of atmospheric plasma-sprayed LSM/YSZ composite cathode materials, J. Therm. Spray. Tech. 16 (2007) 1005–1010.
[52] S.L. Zhang, C.X. Li, C.J. Li, Plasma-sprayed Y_2O_3-stabilized ZrO_2 electrolyte with improved interlamellar bonding for direct application to solid oxide fuel cells, J. Fuel Cell Sci. Tech. 11 (2014).
[53] C.J. Li, X.J. Ning, C.X. Li, Effect of densification processes on the properties of plasma-sprayed YSZ electrolyte coatings for solid oxide fuel cells, Surf. Coat. Tech. 190 (2005) 60–64.
[54] C. Zhang, W.Y. Li, M.P. Planche, C.X. Li, H.L. Liao, C.J. Li, C. Coddet, Study on gas permeation behaviour through atmospheric plasma-sprayed yttria stabilized zirconia coating, Surf. Coat. Tech. 202 (2008) 5055–5061.
[55] F. Ahmed, K. Bayerlein, S.M. Rosiwal, M. Goken, K. Durst, Stress evolution and cracking of crystalline diamond thin films on ductile titanium substrate: analysis by micro-Raman spectroscopy and analytical modelling, Acta Mater. 59 (2011) 5422–5433.
[56] U.A. Handge, Analysis of a shear-lag model with nonlinear elastic stress transfer for sequential cracking of polymer coatings, J. Mater. Sci. 37 (2002) 4775–4782.
[57] H.B. Guo, S. Kuroda, H. Murakami, Microstructures and properties of plasma-sprayed segmented thermal barrier coatings, J. Am. Ceram. Soc. 89 (2006) 1432–1439.
[58] A.D. Jadhav, N.P. Padture, E.H. Jordan, M. Gell, P. Miranzo, E.R. Fuller, Low-thermal-conductivity plasma-sprayed thermal barrier coatings with engineered microstructures, Acta Mater. 54 (2006) 3343–3349.
[59] Y.Z. Xing, C.J. Li, Q. Zhang, C.X. Li, G.J. Yang, Influence of microstructure on the ionic conductivity of plasma-sprayed yttria-stabilized zirconia deposits, J. Am. Ceram. Soc. 91 (2008) 3931–3936.
[60] F. Kroupa, J. Dubsky, Pressure dependence of Young's moduli of thermal sprayed materials, Scr. Mater. 40 (1999) 1249–1254.
[61] W.X. Zhang, T.J. Wang, L.X. Li, Numerical analysis of the transverse strengthening behavior of fiber-reinforced metal matrix composites, Comp. Mater. Sci. 39 (2007) 684–696.